Quantitative 3D Investigation of Nanoparticle Assemblies by Volumetric Segmentation of Electron Tomography Datasets

*Safiyye Kavak [a], Ajinkya Anil Kadu [a,b], Nathalie Claes [a], Ana Sánchez-Iglesias [c], Luis M. Liz-Marzán [c,d,e,f], Kees Joost Batenburg [b,g], Sara Bals [a]**

[a]EMAT, University of Antwerp, Groenenborgerlaan 171, 2020 Antwerp, Belgium.

[b]Computational imaging group, Centrum Wiskunde & Informatica (CWI), Science Park 123, 1098 XG, Amsterdam, The Netherlands

[c]CIC biomaGUNE, Basque Research and Technology Alliance (BRTA), Paseo de Miramón 194, 20014 Donostia – San Sebastián, Spain

[d]Centro de Investigación Biomédica en Red, Bioingeniería, Biomateriales y Nanomedicina (CIBER-BBN), Paseo de Miramón 194, 20014 Donostia – San Sebastián, Spain

[e]Ikerbasque, Basque Foundation for Science, 48009 Bilbao, Spain

[f]Cinbio, Universidade de Vigo, 36310 Vigo, Spain

[g]Leiden Institute of Advanced Computer Science (LIACS), Leiden University, Niels Bohrweg 1, 2333 CA, Leiden, The Netherlands

KEYWORDS: nanoparticle assemblies, hybrid nanoparticles, electron tomography, segmentation, Watershed transform, spherical Hough transform

Abstract

Morphological characterization of nanoparticle assemblies and hybrid nanomaterials is critical in determining their structure-property relationships, as well as in the development of structures with desired properties. Electron tomography (ET) has become a widely utilized technique for the three-dimensional characterization of nanoparticle assemblies. However, the extraction of quantitative morphological parameters from the reconstructed volume can be a complex and labor-intensive task. In this study, we aim to overcome this challenge by automating the volumetric segmentation process applied to three-dimensional (3D) reconstructions of nanoparticle assemblies. Key to enabling automated characterization is to assess the performance of different volumetric segmentation methods in accurately extracting predefined quantitative descriptors for morphological characterization. In our methodology, we compare the quantitative descriptors obtained through manual segmentation with those obtained through automated segmentation methods, to evaluate their accuracy and effectiveness. To show generality, our study focuses on the characterization of assemblies of CdSe/CdS quantum dots, gold nanospheres (AuNSs) and CdSe/CdS encapsulated in polymeric micelles, and silica-coated gold nanorods (AuNRs) decorated with both CdSe/Cds or PbS quantum dots. We use two unsupervised segmentation algorithms: the Watershed transform and the spherical Hough transform. Our results demonstrate that the choice of automated segmentation method is crucial for accurately extracting the predefined quantitative descriptors. Specifically, the spherical Hough transform exhibits superior performance in accurately extracting quantitative descriptors, such as particle size and interparticle distance, thereby allowing for an objective, efficient, and reliable volumetric segmentation of complex nanoparticle assemblies.

1. Introduction

Nanoparticle assemblies with tunable three-dimensional (3D) structures and properties are of great interest in various fields.[1–4] By altering the number, shape, size, and separation distance between individual nanoparticles, it is possible to assemble custom structures with specific properties for targeted use.[5] Of particular interest are multifunctional nanostructures comprising particles with different compositions.[6] However, a detailed understanding of the structure-property relationship often requires a thorough structural characterization that provides accurate information about the distribution and mutual separation between the different components. For example, when combining plasmonic nanoparticles with photoluminescent quantum dots, the overall optical response critically depends on their precise organization, which may result in photoluminescence quenching or enhancement, for shorter or longer separation distances.

Transmission electron microscopy (TEM) is a widely used technique for studying the shape, size distribution, composition, and structure of nanomaterials. However, conventional TEM images only provide a two-dimensional (2D) representation of a three-dimensional (3D) object. One way to overcome this limitation is through electron tomography (ET), which involves acquiring a series of 2D projection images at different angles and using them to create a 3D reconstruction. This method has proven to be particularly useful for characterizing 3D assemblies of nanoparticles. Significant progress has been recently made toward optimizing the acquisition and reconstruction of ET tilt series.[7–15] Still, reconstruction artifacts, such as misalignment, streak artifacts, or the missing wedge,[16] hamper straightforward extraction of quantitative morphological parameters, such as e.g., the number of particles, and the interparticle distances, from a reconstructed 3D tomography volume.

To extract quantitative morphological parameters from a 3D reconstructed volume, volumetric segmentation is essential. This process involves assigning regions of the data set to specific materials or compositions based on the grey levels of the voxels. Many approaches have been proposed to reach this goal, among which manual segmentation is most often used. This process involves visually identifying the boundary between different grey levels in a 3D reconstructed volume. Ideally, the procedure is repeated for each slice of the reconstructed volume in the three principal directions (x, y, z). Manual segmentation of 3D reconstructions of nano-assemblies presents a challenge in terms of accuracy and efficiency. The subjective nature of manual segmentation and the difficulty in segmenting assemblies with a high number of small or closely spaced particles are the major drawbacks. To address these limitations, advanced reconstruction algorithms have been developed. One such example is the discrete algebraic reconstruction technique (DART),[17–19] which assumes the sample consists of a small, discrete set of materials. While effective in certain cases, this method requires extensive parameter tuning and is susceptible to image formation artifacts. Another example is the sparse sphere reconstruction (SSR) method, which assumes that nanoparticles can be modelled as perfect spheres of known size.[10] Although suitable for many nanoparticle assemblies, this algorithm cannot be generalized for assemblies made of anisotropic nanoparticles.

Considering the limitations of existing methods, the focus of the present study is on enabling automated volumetric segmentation for quantitative morphological feature extraction of 3D nanoparticle assemblies, using robust image processing operations, and therefore not relying on the limiting assumptions of advanced reconstruction methods. Key to our approach is determining which automated volumetric segmentation methods are suitable for accurately extracting predefined quantitative descriptors for morphological characterization. This requires a rigorous

validation of algorithmic performance with respect to a "gold standard" segmentation. In our methodology, we evaluate the accuracy of automated volumetric segmentation methods by comparing the quantitative descriptors obtained through manual segmentation with those obtained through automated segmentation.

Specifically, our experimental study is devoted to extracting quantitative parameters that describe 3D assemblies based on the assembly of cadmium selenide/cadmium sulfide (CdSe/CdS) quantum dots (QDs) and co-assembly of spherical gold nanoparticles (AuNPs) and CdSe/CdS, both encapsulated in polymeric micelles of polystyrene-polyacrylic acid (PS-PAA), induced by hydrophobic interactions (**Figure 1**). We also investigated hybrid materials comprising silica-coated gold nanorods (AuNRs@SiO_2) decorated with QDs (CdSe/CdS and PbS), (**Figure 2**). These systems are of interest because the combination of semiconductor and plasmonic materials may enhance existing functionalities or may even lead to new synergy and applications in the fields of catalysis,[20,21] plasmonics[22–25] sensors,[26] and cancer therapy.[27]

Two different strategies were used here, which can be applied toward tailoring the interaction between the plasmonic Au core and the satellite QDs, through control over their respective positions and distances. Whereas in the first strategy, hydrophobic NPs were encapsulated into block-copolymer micelles upon the addition of water, the second involved silica coating of Au NRs and chemical binding of QDs onto the thiol-functionalized silica surface.

Our study compares the extraction of fixed quantitative descriptors, including the number of QDs, particle size, and interparticle distance, from 3D reconstructions through manual segmentation, with the results obtained using unsupervised image segmentation methods. We use two alternative unsupervised algorithms for segmentation: the Watershed transform[28] and the spherical Hough transform.[29]

The Watershed transform has been traditionally employed for volumetric segmentation,[30] and it has been successfully demonstrated in quantifying spherical silica NPs from electron tomography reconstructions. However, this method may fail in certain scenarios due to its sensitivity to noise, over-segmentation, and difficulty in separating touching or overlapping objects.[31] In contrast, it was recently shown that the spherical Hough transform can address some of these limitations, delivering more accurate and reliable results when extracting quantitative descriptors.[32] We observe that the spherical Hough transform has found applications in biomedical imaging,[33,34] but has not been demonstrated in 3D electron tomography to best of our knowledge. While both the Watershed transform and the spherical Hough transform can perform on par with manual segmentation techniques for the characterization of nanoparticle assemblies, a comparative analysis of the number of particles in the assembly, their average diameter, and interparticle distances, reveals that the spherical Hough transform surpasses the Watershed transform in terms of accuracy and efficiency. The Hough approach therefore offers a robust, objective, and efficient method for the volumetric segmentation of diverse nanoparticle assemblies.

2. Materials and Methods

2.1. Materials and Synthesis Details

Samples described in **Table 1**.

Table 1. Description of the samples used in this study.

Sample	Core	QDs	Encapsulated/Assembled
#1	-	CdSe/CdS	Polymeric micelles
#2	Au nanosphere	CdSe/CdS	Polymeric micelles

#3	Au nanorod	CdSe/CdS	SiO_2 shell
#4	Au nanorod	PbS	SiO_2 shell

2.1.1. Chemicals

Gold (III) chloride trihydrate ($HAuCl_4 \cdot 3H_2O$, ≥ 99%), sodium borohydride ($NaBH_4$, 99%), L-ascorbic acid (AA, ≥ 99%), silver nitrate ($AgNO_3$, ≥ 99%), sodium oleate (NaOL, ≥ 99%), tetraethyl orthosilicate (TEOS, 98%), sodium hydroxide (NaOH, 97%), benzyldimethylhexadecylammonium chloride (BDAC), hexadecyltrimethylammonium bromide (CTAB, ≥ 99%), hexadecyltrimethylammonium chloride (CTAC, 25 %wt), tetrahydrofuran (THF, ≥ 99.9%), and 3-mercaptopropyl-trimethoxysilane (MPTS, 95 %) were purchased from Sigma-Aldrich. Hydrochloric acid solution (HCl, 37 wt%) and ethanol (99.5 %) were purchased from Scharlau. Thiol-terminated polystyrene (PS509-SH, MW: 53K) and poly (styrene-b-acrylic acid) (PS403-b-PAA62) were purchased from Polymer Source. Quantum dot nanocrystals stabilized with oleic acid (OA) in tetrahydrofuran: CdSe/CdS@OA (diameter: 11.4 ± 1.8 nm) and PbS@OA (diameter: 6.2 ± 0.6 nm) were purchased from Center for Applied Nanotechnology GmbH (CAN). All chemicals were used without further purification. Milli-Q water (resistivity 18.2 MΩ·cm at 25 °C) was used in all experiments. All glassware was cleaned with aqua regia, rinsed with Milli-Q water, and dried before use.

2.1.2. Synthesis of gold nanospheres.[7]

Gold nanospheres were synthesized via successive seed-mediated growth. First, gold seeds were prepared by fast reduction of $HAuCl_4$ with $NaBH_4$ in CTAB solution. $HAuCl_4$ solution (0.025 mL, 50 mM) solution was added to a solution of CTAB (4.7 mL, 100 mM), the mixture was stirred for

5 min at 27 °C until the Au^{+3}:CTAB complex was solubilized. Subsequently, a freshly prepared $NaBH_4$ solution (0.3 mL, 10 mM) was rapidly injected under vigorous stirring. The solution color changed from yellow to brownish yellow and stirring was stopped after 2 min. The Au seed solution was aged at room temperature for 30 min prior to use, to allow the decomposition of excess sodium borohydride. The final concentration of metallic gold was 0.25 mM. The same seed solution was used to synthesize Au nanospheres and Au nanorods.

An aliquot of seed solution (0.6 mL) was added to a growth solution (100 mL) containing CTAC (100 mM), $HAuCl_4$ (0.18 mM), and AA (0.36 mM). The mixture was left undisturbed for 2 h at 25 ºC. After synthesis, the colloidal dispersion containing 10 nm gold nanospheres was centrifuged (9000 rpm, 2 h) to remove excess CTAC and ascorbic acid, and redispersed in an aqueous BDAC solution (10 mM) to a final Au concentration equal to 2.5 mM.

To grow 10 nm Au nanospheres up to 40 nm, a volume of Au seed solution (0.08 mL, 2.5 mM) was added under vigorous stirring to a growth solution (25 mL) containing BDAC (100 mM), $HAuCl_4$ (0.5 mM), and AA (1 mM). The mixture was left undisturbed for 30 min at 30 ºC, and then washed twice by centrifugation. The particles were finally dispersed in CTAB (1 mM) to a final Au concentration equal to 5 mM. The final diameter of Au spheres was 38 ± 1 nm.

2.1.3 Synthesis of gold nanorods.[35]

Gold nanorods (AuNRs) were prepared through the well-known seeded growth method, based on the reduction of $HAuCl_4$ on CTAB-stabilized Au nanoparticle seeds in the presence of silver ions.

To prepare the growth solution, 1.8 g of CTAB and 0.25 g of NaOL were dissolved in 100 mL of warm Milli-Q water (~ 50 ºC), in a 250 mL erlenmeyer flask. Once NaOL was completely

dissolved, the mixture was cooled down to 30 ºC and $AgNO_3$ (4.8 mL, 4 mM) was added under stirring. The mixture was kept at 30 ºC for 15 min, after which $HAuCl_4$ was added (1 mL, 50 mM) under vigorous stirring. The mixture became colorless after 20 min at 30 ºC and HCl (0.3 mL, 37%) was introduced. After 15 min of stirring, AA (0.25 mL, 64 mM) was added, and the solution was vigorously stirred for 30 s. Finally, seed solution (0.16 mL, 0.25 mM) was injected into the growth solution under vigorous stirring for 5 minutes, and then the solution was left undisturbed at 30 ºC for 12 h. The solution was centrifuged twice (7000 rpm, 30 min) to remove excess reactants and dispersed in aqueous CTAB solution (1 mM). The final concentration of metallic Au was 5 mM. The final dimensions of AuNRs were 88 ± 3 nm (length) and 22 ± 1 nm (width).

2.1.4 Functionalization with polystyrene, clustering, and encapsulation of Au and CdSe/CdS nanoparticles.[7,36]

To replace the surfactant with a hydrophobic polymer, thiolated polystyrene (PS-SH) with a molecular weight of 53 kg/mol was used. The AuNS dispersion (2 mL, 5 mM) was added dropwise under sonication to a PS-SH solution (1 molecule of PS-SH per nm^2 of gold surface) in THF (20 mL). The solution was left for 15 min in an ultrasonic bath. To ensure ligand exchange, the resulting mixture was left undisturbed for 12 h, and then centrifuged twice (7000 rpm, 30 min). The particles were finally dispersed in THF to a final Au concentration of 5 mM.

The clustering of PS-functionalized Au NPs (AuNPs@PS) and CdSe/CdS@OA quantum dots was carried out according to a previously reported method. In a typical self-assembly experiment, water (0.2 mL) was added dropwise to AuNP@PS (0.25 mM, 10 mL) and CdSe/CdS@OA (0.02 mL, 10 mg/mL) in THF, under magnetic stirring. The dispersion was stirred for 5 min and then a solution of PS403-b-PAA62 in THF (1 mL, 6 mg/mL) was added dropwise under magnetic stirring.

Subsequently, the water content was increased up to 35 wt%, followed by increasing the temperature up to 70 ºC, which was maintained for 30 min. The dispersion of clusters was then centrifuged twice (4000 rpm, 30 min) and redispersed in water.

For clustering of CdSe/CdS@OA quantum dots, water (0.3 mL) was added dropwise to the QDs dispersion (0.02 mL, 10 mg/mL) in THF, under magnetic stirring. The mixture was stirred for 10 min and then a solution of PS403-b-PAA62 in THF (0.2 mL, 6 mg/mL) was added dropwise under magnetic stirring. Subsequently, the water content was increased up to 35 wt%, followed by increasing the temperature up to 70 ºC, which was maintained for 30 min. The clusters dispersion was centrifuged twice (18000 rpm, 30 min) and redispersed in water.

2.1.5. Mesoporous silica coating of AuNRs and decoration with QDs.[37]

Mesoporous silica shells were grown on AuNRs by adding three consecutive aliquots of TEOS solution (24 µL, 20 vol% in EtOH) at 60 min intervals, to a solution containing AuNRs@CTAB (8 mL, 1 mM) and NaOH (80 µL, 100 mM) in CTAB (1.5 mM). The reaction was allowed to continue while stirring for 2 days. The resulting silica-coated gold nanorods (AuNRs@SiO_2) were washed twice with ethanol (5000 rpm, 30 min), and finally dispersed in EtOH to a final Au concentration of 1 mM. Then, MPTS (5 mL, 0.15 % v/v) was added to the AuNRs@SiO_2 (5 mL, 1 mM) dispersion, to modify the silica surface. The mixture was heated to 40 °C for 24 hours and then thiol-functionalized AuNRs@SiO_2 were washed three times with ethanol by centrifugation to remove excess MPTS, and finally dispersed in THF to a final Au concentration of 0.5 mM.

CdSe/CdS or PbS QDs dispersed in THF (0.1 mL, 10 mg/mL) were mixed with the suspension of thiol-functionalized AuNRs@SiO_2 nanoparticles in THF (5 mL, 0.5 mM) under mild stirring for 4 hours. The QDs were self-assembled onto AuNRs@SiO_2 nanoparticles due to the interaction of

thiol groups and QDs. Finally, the hybrid AuNRs@SiO_2@QDs nanoparticles were centrifuged twice and redispersed in THF.

2.2 Methods

2.2.1. TEM Imaging

TEM images were acquired with a JEOL JEM-1400PLUS transmission electron microscope operating at an acceleration voltage of 120 kV.

2.2.2. Electron Tomography

The ET experiments for samples #1, #2, and #3 were performed using a Thermo Fisher Tecnai G2 microscope operating at 200 kV in high-angle annular dark field (HAADF-STEM) mode. Tilt series for sample #1 were acquired from -72° to +75°, for sample #2 from -75° to +75°, and for sample #3 from -66° to +69°. Sample #4 contained smaller quantum dots (QDs) compared to the other three samples. Therefore, a Thermo Fisher Scientific Tecnai Osiris operating at 200 kV with the better spatial resolution was used to collect a tilt series from -75° to +75°. A Fischione model 2020 single tilt tomography with a tilt increment of 3° was used for all series. From these tilt-series, 3D volumes were reconstructed using the Expectation Maximization algorithm,[38–40] which iteratively minimizes the maximum likelihood of the mismatch between the forward projection and the tilt-series, assuming that the noise follows a Poisson distribution, which is appropriate for electron microscopy images. During each iteration, the algorithm first estimates the hidden parameters of the model using the current estimates of the observed parameters and then updates the estimates of the observed parameters using the newly-estimated hidden parameters. This process is repeated until convergence, resulting in a 3D volume with minimal noise and artifacts.

2.2.3 Watershed transform

The Watershed transform is a prevalent technique in the field of image processing for demarcating different regions or "basins" in an image. This method is based on the principles of a "watershed", which is a region of land that drains water into a specific river or lake. In the context of image processing, the idea behind Watershed segmentation is to treat the grayscale values in an image as a topographical map, where the darkest voxels represent the low points (valleys), and the lightest voxels represent the high points (peaks). The algorithm then "floods" the 3D image from the peaks, filling in the valleys and creating a set of connected regions. These regions can then be labelled and treated as individual particles in the image. Details about the method and its hyperparameters are given in the **SI-section 2**. In this study, the Watershed transform was implemented using Avizo3D visualization software, and the LabelAnalysis tool of Avizo3D was used to quantify morphological parameters, including center position and corresponding radius.

2.2.4 Spherical Hough transform

The spherical Hough transform is an algorithm that detects spherical objects in the 3D image, characterized by a radius and a central position (as shown in **SI-section 3**). [41,42] This approach has been primarily utilized in biomedical imaging for segmentation purposes, such as detecting multiform femoral heads and cell nuclei.[43–45] In our study, the spherical Hough Transform was employed to identify spherical particles in 3D anisotropic assemblies. The four-dimensional representation (i.e., center location and radius) allowed for easier manipulation of the spherical objects in three dimensions. The transform employs a voting mechanism to detect clusters of points that correspond to individual particles and construct a spherical model of the particles using these clusters (refer to the **SI-section 3** for more information regarding the algorithm). The spherical

Hough Transform offers several benefits over alternative methods, including robustness to noise and the ability to handle complex shapes. Its voting system allows for the accurate detection of particles even in the presence of noise or distortion, thereby enabling the separation of attached and/or agglomerated particles without subjectivity. The implementation of this transform was performed in MATLAB, and the resulting code was validated on numerous synthetic structures.

3. Results

In **Figure 3**, an overview of the different samples is presented through 2D high-angle annular dark-field scanning transmission electron microscopy (HAADF-STEM) images. Sample #1, depicted in **Figure 1.a** and **Figure 3.a**, comprises solely of CdSe/CdS QDs embedded within a polymeric micelle shell. Sample #2, shown in **Figure 1.b** and **Figure 3.b**, was prepared by co-assembly of AuNPs and QDs,[7,35–37] resulting in hybrid assemblies typically containing one Au nanosphere and numerous QDs. Two additional samples were examined, which were prepared by the second strategy, as described above. **Figure 2.a** and **Figure 3.c** present the general appearance of the hybrid particles in sample #3, which consist of CdSe/CdS QDs assembled onto gold nanorods and surrounded by a silica shell (AuNRs@SiO_2). Sample #4 (**Figure 2.b** and **Figure 3.d**) has a similar structure, but PbS QDs were used instead of CdSe/CdS.

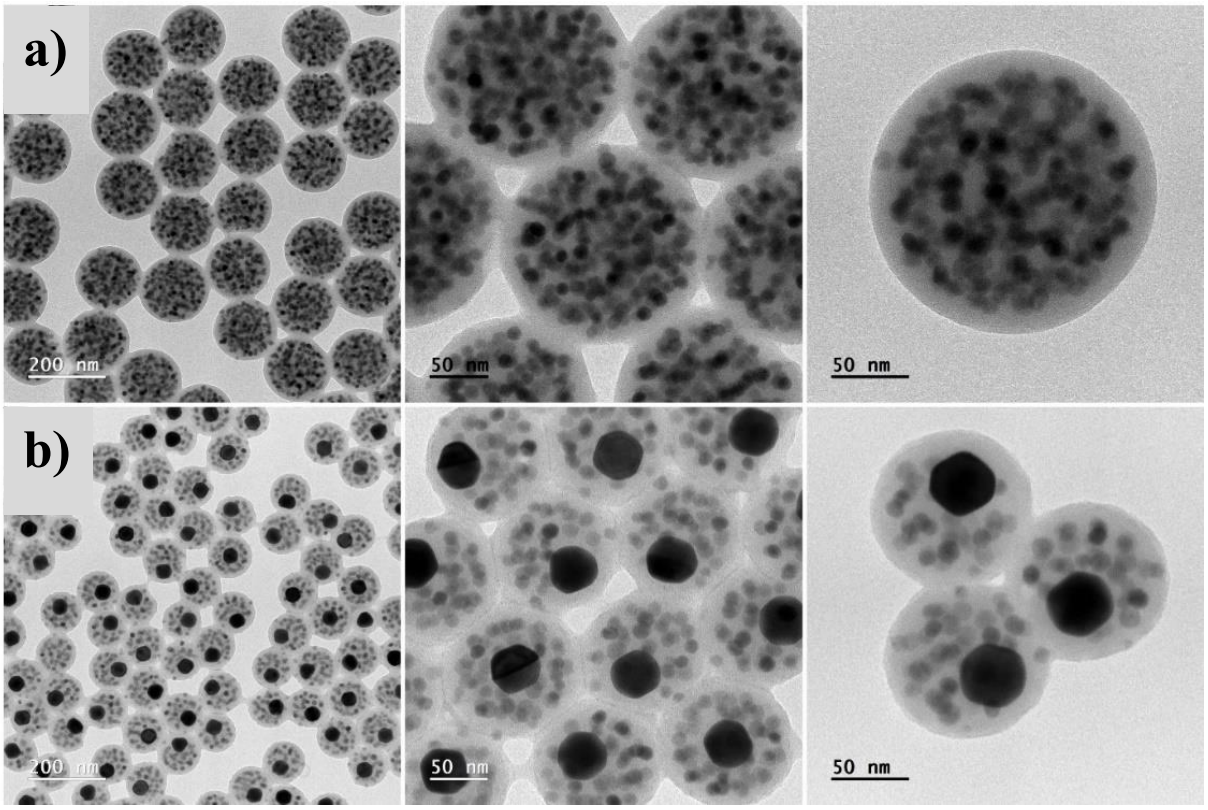

Figure 1. TEM images of clusters encapsulated in polymeric micelles: **a)** CdSe/Cd; **b)** AuNS@CdSe/CdS.

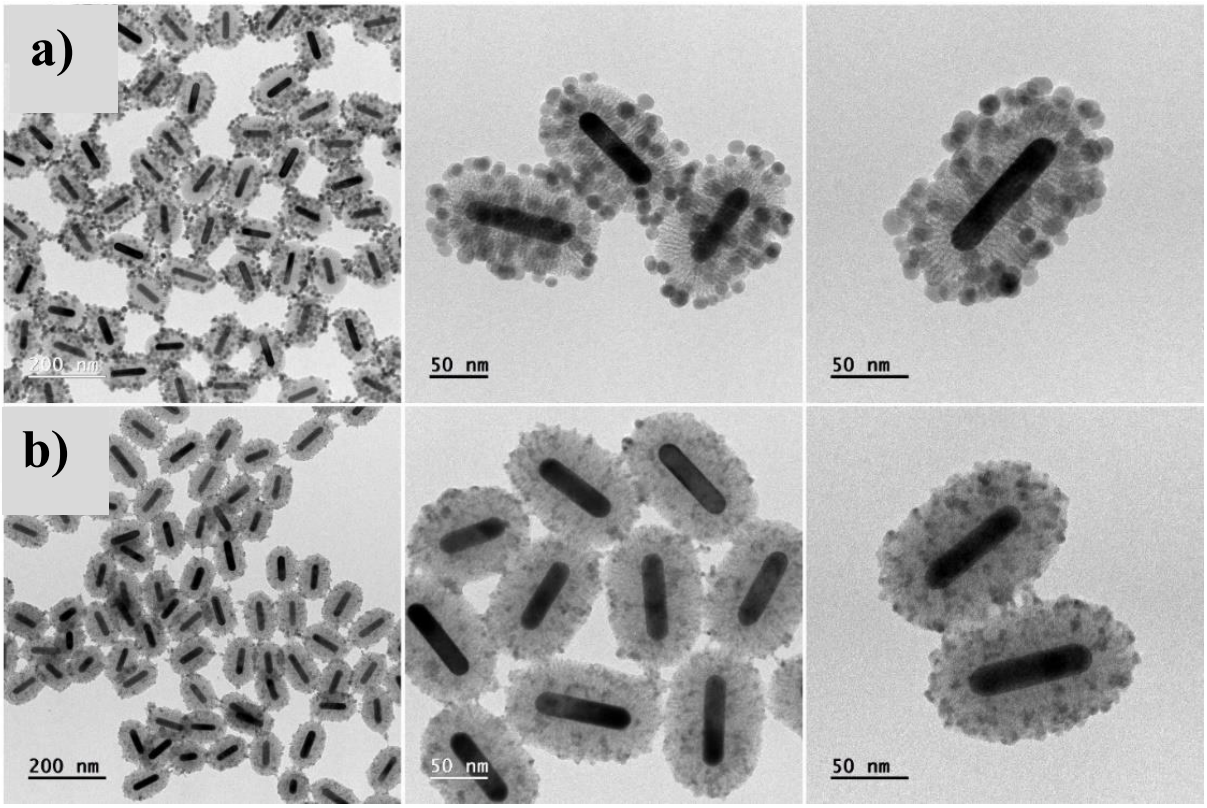

Figure 2. TEM images of AuNR@SiO_2@QDs: **a)** CdS/CdS; **b)** PbS.

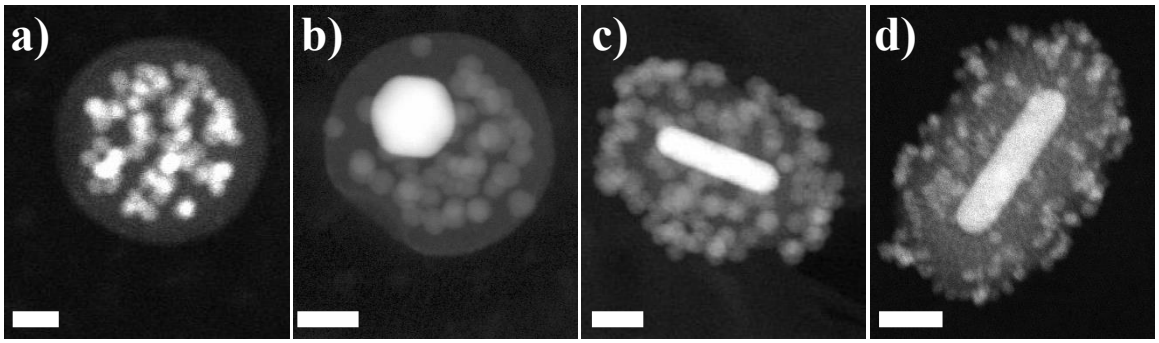

Figure 3. 2D HAADF-STEM images of different hybrid NP assemblies: **a)** sample #1, CdSe/CdS QDs in polymeric micelles; **b)** sample #2, AuNPs and CdSe/CdS co-encapsulated in polymeric micelles; **c)** sample #3, AuNR@SiO_2@CdSe/CdS; **d)** sample #4, AuNR@SiO_2@PbS. All scale bars correspond to 30 nm.

The morphological characterization of all nanoparticle assemblies was performed through the application of ET. The technical details and the parameters used for the ET experiments can be found in the Materials and Methods section. The results of the ET reconstructions are depicted in **Figure 4**, where the visual representation of the 3D structures and representative orthoslices acquired through the 3D reconstructions are presented. Our observations indicate that the Au NPs are positioned at the central axis of the assemblies, with a uniform distribution of the QDs surrounding them. We can also confirm that, the QDs in samples #3 and #4 are primarily located on the outer surface of the SiO_2 shell, whereas in samples #1 and #2, the QDs are dispersed throughout the polymeric micelle matrix. This different distribution of QDs was expected from the application of different synthesis methods, samples #1 and #2 being prepared from co-assembly of NPs from a mixed dispersion and subsequently encapsulated by the block-copolymer, whereas in samples #3 and #4 the QDs were added after coating of AuNRs with the SiO_2 shell and modifying its outer surface to facilitate QD binding.

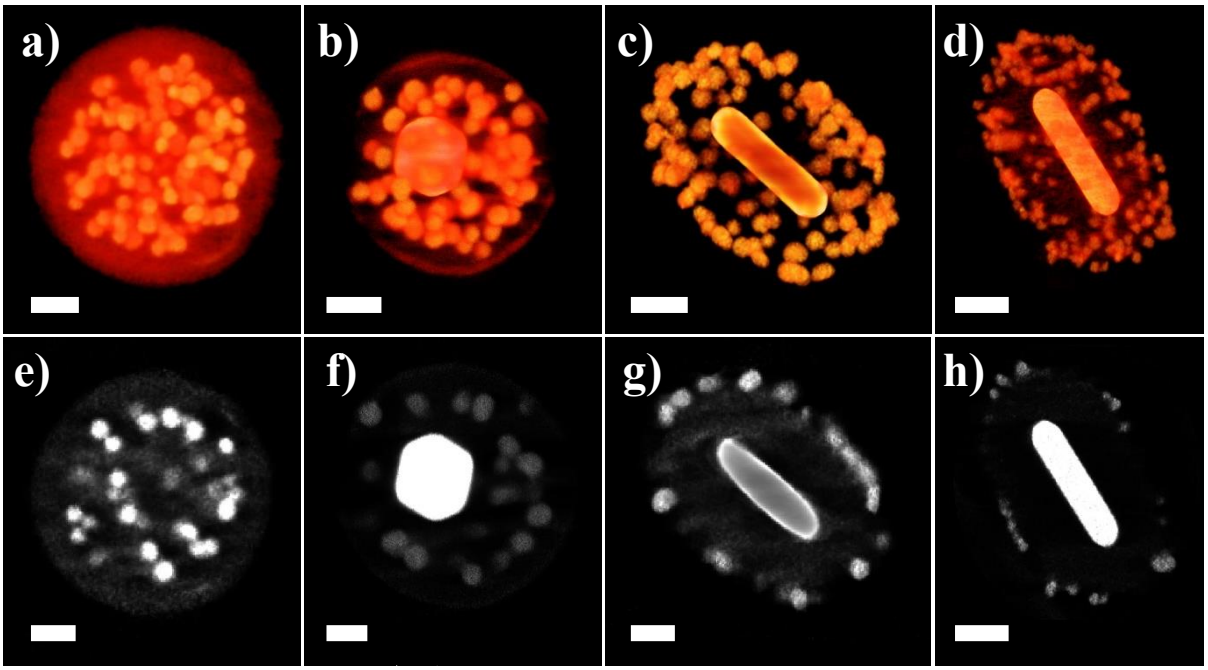

Figure 4. 3D visualizations of representative reconstructions (**a-d: #1-#4**), and orthoslices (**e-h: #1-#4)**. All scale bars represent 30 nm.

The ultimate objective of our 3D analysis was the determination of quantitative descriptors for the nanoparticle assemblies, including the number of particles within the assembly, the interparticle distances between QDs, and the mean diameter of the individual QDs. To obtain these parameters, the center of mass position of each QD must be first determined. However, as the QDs in the assemblies exhibit varying shapes and sizes, and frequently appear to be agglomerated in the reconstructions, algorithms such as DART and SSR are not suitable. Therefore, the focus of this study is to optimize the segmentation process applied to a reconstructed 3D dataset, as it pertains to quantifying the morphological features of nanoparticle assemblies.

First, we performed careful manual segmentation for every orthoslice along the x, y, and z directions. The boundaries of the individual QDs and the Au nanoparticle were manually indicated and separated from the background for each assembly, as illustrated in **Figure S1**. This approach

is time-consuming and can be subjective. To reduce user bias, manual segmentation was repeated several times. In this manner, we consider the resulting quantitative parameters to be the accepted reference values, and they are listed in **Table 2**.

Table 2. Summary of the most important descriptors for the NP assemblies as extracted by means of different segmentation approaches: manual segmentation, use of the Watershed transform, and a spherical Hough transform. The determined descriptors include: the number of QDs in an assembly, the diameter distribution of the individual QDs, the average interparticle distances, and the nearest neighbor distances, together with standard error values.

		Manual seg.	**Watershed transform**	**Spherical Hough transform**
#1	**number of QDs**	136	127	136
	diameter (*nm*)	10.1 ± 0.2	10.6 ± 0.3	10.0 ± 0.1
	average distance (*nm*)	65. 3 ± 0.2	67.7 ± 0.2	65.0 ± 0.2
	nearest neighbor distance (*nm*)	11.6 ± 0.3	12.0 ± 0.3	12.1 ± 0.2
#2	**number of QDs**	71	78	72
	diameter (*nm*)	10.9 ± 0.2	10.2 ± 0.2	11.0 ± 0.1
	average distance (*nm*)	53.7 ± 0.3	53.4 ± 0.3	53.9 ± 0.2
	nearest neighbor distance (*nm*)	14.2 ± 0.6	12.7 ± 0.7	14.6 ± 0.5
#3	**number of QDs**	130	131	128
	diameter (*nm*)	11.7 ± 0.2	11.5 ± 0.2	11.8 ± 0.1
	average distance (*nm*)	75.2 ± 0.2	74.8 ± 0.2	73.6 ± 0.2
	nearest neighbor distance (*nm*)	12.4 ± 0.2	12.6 ± 0.3	12.5 ± 0.2
#4	**number of QDs**	153	154	150
	diameter (*nm*)	6.7 ± 0.1	6.3 ± 0.1	6.5 ± 0.1
	average distance (*nm*)	66.5 ± 0.2	70.3 ± 0.2	70.4 ± 0.2
	nearest neighbor distance (*nm*)	8.2 ± 0.4	8.6 ± 0.3	8.4± 0.3

Next, we performed segmentation of our 3D reconstructions based on the use of a Watershed transform[31] (**Figure S2-3**), as summarized in **Table 2**, and **Figure 5**. The percentage error values for the calculated parameters are presented in **Figure 6**. It can be seen that the quantified results are in reasonable agreement with the manual segmentation results, which we accepted as accepted reference values. The obtained diameters are furthermore consistent with the values provided by the vendor of the quantum dot nanocrystals (see section 4.1.1). On the other hand, larger deviations (see error bars) were found regarding the number of QDs per assembly for samples #1 and #2, average diameter for samples #1, #2, and #4, and nearest neighbor distance for samples #2 and #4. This unexpected result (in particular for QD diameter) is likely to result from an oversegmentation problem, which we discuss below.

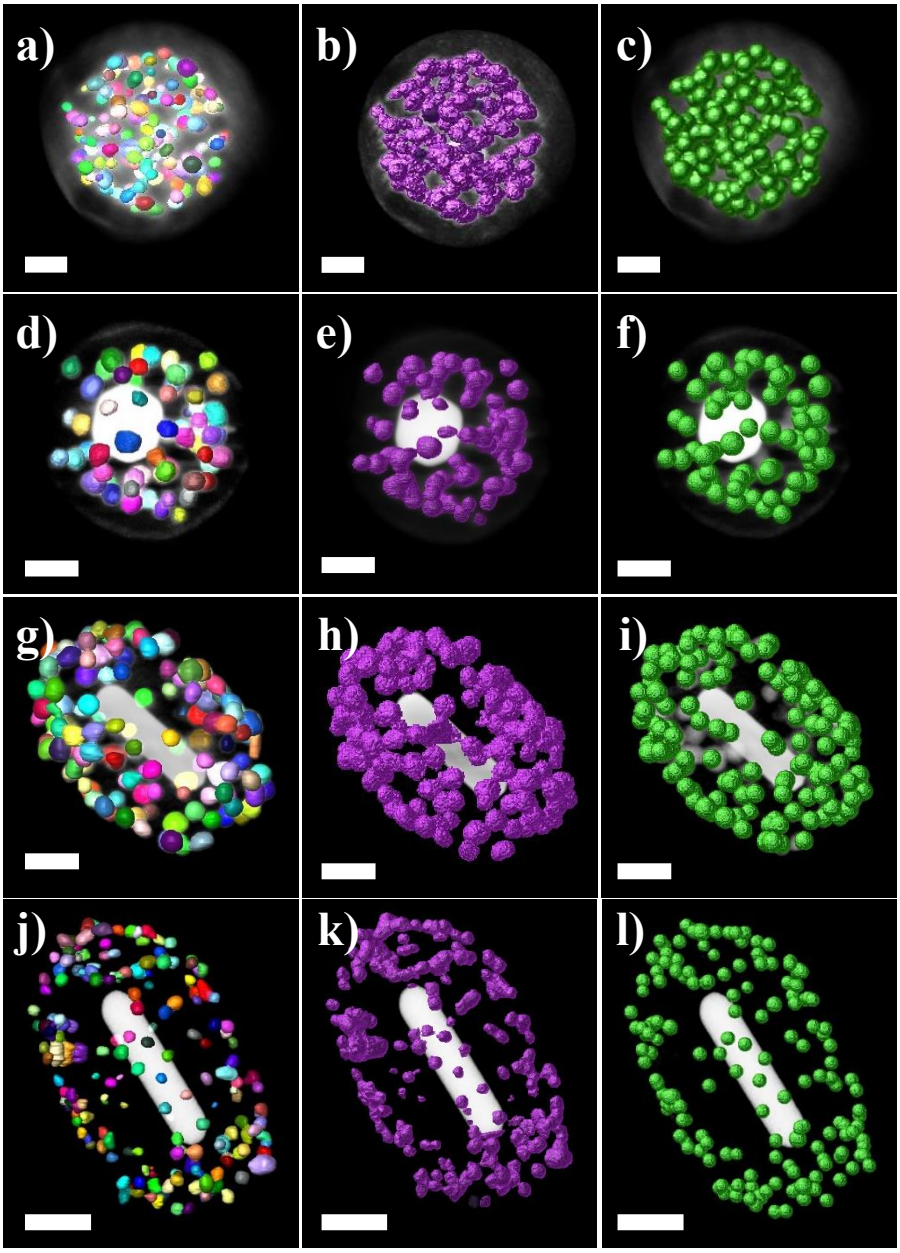

Figure 5. 3D visualizations obtained through manual segmentation **(a, d, g, j)**, segmentation using the Watershed transform **(b, e, h, k)**, and segmentation using the spherical Hough transform **(c, f, i, l),** for samples #1, #2, #3, and #4, from first to last row, respectively. Scale bars represent 30 nm in each image.

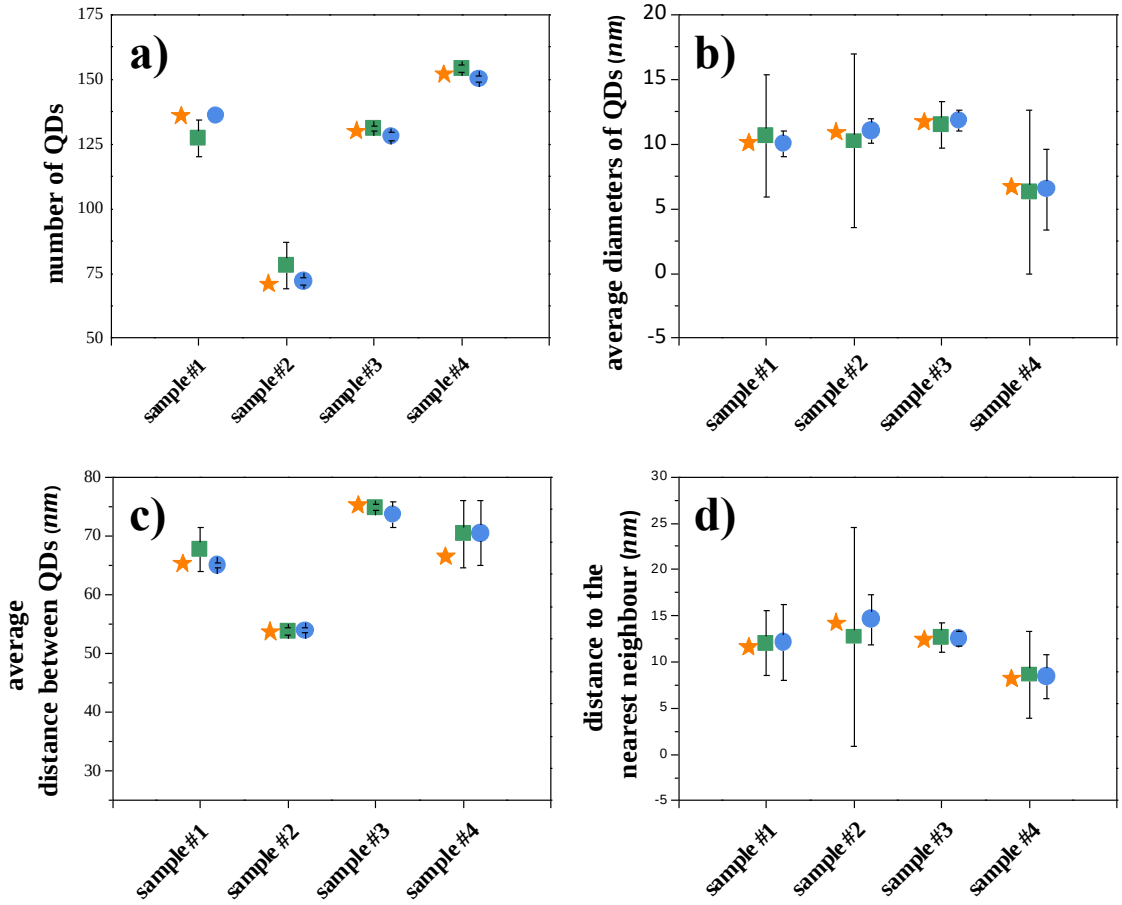

Figure 6. Percentage error values for: **a)** number of QDs, **b)** average diameters of QDs, **c)** average distance between QDs, and **d)** average distance of a QD to the nearest neighbor QD. Stars (★) indicate manual segmentation results, squares (■) indicate the Watershed transform results, and circles (●) indicate the results from the spherical Hough function. Error bars were calculated from the difference (%) to the average of accepted reference values (manual segmentation).

As an alternative, we applied the spherical Hough transform and a qualitative comparison to the manual segmentation and results obtained by the Watershed transform is depicted in **Figure 5**. The quantified outcomes are illustrated in **Table 2** and represented by the error percentage values in **Figure 6**. The analysis reveals that the quantified results obtained through the spherical Hough

transform segmentation exhibit a high degree of concurrence with the reference data. The number of QDs demonstrates excellent overlap with the reference data, as demonstrated by the small error percentage values displayed in **Figure 6**. In comparison to the results obtained through the Watershed transform, the spherical Hough transform exhibits significantly improved accuracy in determining the parameters of average diameter, average distance, and average nearest neighbor distance, as evidenced by the results in **Figure 6**.

4. Discussion

The efficacy of each segmentation method was compared across four distinct nanoparticle assemblies. The applied methods comprised manual segmentation, the Watershed transform, corresponding to a traditional approach for segmentation problems and the spherical Hough transform, an alternative technique for segmentation[32]. Our results indicate 136, 71, 130, and 152 particles were detected by manual segmentation for samples #1 – #4, respectively. The number of particles detected using the Watershed transform was higher than the accepted reference values for samples #2, #3, and #4, an issue commonly referred to as over-segmentation (**Figure S4**), which arises from the division of an image of particles into an excessive number of regions or segments that do not correspond to distinct structures or particles. Conversely, the number of particles detected using the Spherical Hough transform was in better agreement (lower percentage error values, **Figure 6**) with the accepted reference values, compared to the Watershed transform, for all samples.

Subsequently, the diameters of the nanoparticles were computed using the three segmentation methods. The diameters computed through manual segmentation were 10.1, 10.9, 11.7 and 6.7 nm for samples #1 – #4, respectively. The diameters calculated using the Watershed transform differed from the accepted reference values by 2-7%. In contrast, the diameters calculated using the

Spherical Hough transform again exhibited better agreement with the accepted reference values, with differences ranging from 0.9-3.0%.

Additionally, the inter-particle distances were calculated using all three segmentation methods. The average inter-particle distances calculated through manual segmentation were 65.3, 53.7, 75.2 and 66.5 nm for samples #1 – #4, respectively. The average distances computed using the Watershed transform were different from the accepted reference values by 0.5-3.7% for samples #1-#3, and by 5.7% for sample #4. On the other hand, the average distances computed using the Spherical Hough transform demonstrated improved agreement with the accepted reference values for all samples, with differences ranging from 0.4-2% for samples #1 – #3. And for sample #4, the difference was similar with Watershed transform #4 by 5.8% (**Figure 6**).

The final parameter evaluated was the average nearest neighbor distance, which quantifies the proximity of a nanoparticle to its closest neighboring particle. The average nearest neighbor distances obtained from manual segmentation were 11. 6 nm, 14.2 nm, 12.4 nm, and 8.2 nm for samples #1 – #4, respectively. For sample #1, the average nearest neighbor distance calculated using the spherical Hough transform showed a slightly higher error of 4.3% compared to the Watershed transform, which showed an error of 3.4%. However, for samples #2 – #4, the spherical Hough transform demonstrated improved agreement with manual segmentation results, by 0.8-2.8% difference, compared to the Watershed transform which shows 1.6-10.6% difference, as evident from the data presented in **Figure 6**.

In conclusion, we have performed ET experiments on a collection of nanoparticle assemblies, and evaluated two computational methods for automated volumetric segmentation, the Watershed transform, and the spherical Hough transform, alongside manual segmentation, the latter of which

served as the accepted reference value. Our numerical results indicate that the spherical Hough transform is a superior approach for quantifying 3D nanoparticle assemblies, due to its ability to deliver objective, efficient, and accurate quantification results.

ASSOCIATED CONTENT

Supporting Information.

The following files are available free of charge.

Details of manual segmentation, Watershed transform, and spherical Hough transform. (PDF)

AUTHOR INFORMATION

Corresponding Author

*sara.bals@uantwerpen.be

Author Contributions

The manuscript was written through contributions of all authors. All authors have given approval to the final version of the manuscript.

ACKNOWLEDGMENT

Authors acknowledge financial support from the European Commission under the Horizon 2020 Programme by ERC Consolidator grant no. 815128 (REALNANO). S.K. acknowledges the Flemish Fund for Scientific Research (FWO Vlaanderen) through a PhD research grant (1181122N). L.M.L.-M. acknowledges funding from the European Union's Horizon 2020 research and innovation programme under grant agreement No 861950, project POSEIDON.

REFERENCES

(1) Hanske, C.; Sanz-Ortiz, M. N.; Liz-Marzán, L. M. Silica-Coated Plasmonic Metal Nanoparticles in Action. *Adv. Mater.* **2018**, *30*, 1707003.

(2) Liz-Marzán, L. M. *Colloidal Synthesis of Plasmonic Nanometals*; Ed.; Jenny Standford Publishing: Singapore, 2020.

(3) Scarabelli, L.; Schumacher, M.; Jimenez de Aberasturi, D.; Merkl, J. P.; Henriksen-Lacey, M.; Milagres de Oliveira, T.; Janschel, M.; Schmidtke, C.; Bals, S.; Weller, H.; et al. Encapsulation of Noble Metal Nanoparticles through Seeded Emulsion Polymerization as Highly Stable Plasmonic Systems. *Adv. Funct. Mater.* **2019**, *29,* 1809071.

(4) Mychinko, M.; Skorikov, A.; Albrecht, W.; Sánchez-Iglesias, A.; Zhuo, X.; Kumar, V.; Liz-Marzán, L. M.; Bals, S. The Influence of Size, Shape, and Twin Boundaries on Heat-Induced Alloying in Individual Au@Ag Core–Shell Nanoparticles. *Small* **2021**, *17,* 2102348.

(5) Hollingsworth, J. A.; Htoon, H.; Piryatinski, A.; Götzinger, S.; Sandoghdar, V. When Excitons and Plasmons Meet: Emerging Function through Synthesis and Assembly. *MRS Bull.* **2015**, *40*, 768–776.

(6) de la Encarnación, C.; Jimenez de Aberasturi, D.; Liz-Marzán, L. M. Multifunctional Plasmonic-Magnetic Nanoparticles for Bioimaging and Hyperthermia. *Adv. Drug Deliv. Rev.* **2022**, *189*, 114484.

(7) Sánchez-Iglesias, A.; Grzelczak, M.; Altantzis, T.; Goris, B.; Pérez-Juste, J.; Bals, S.; Van Tendeloo, G.; Donaldson, S. H.; Chmelka, B. F.; Israelachvili, J. N.; et al. Hydrophobic Interactions Modulate Self-Assembly of Nanoparticles. *ACS Nano* **2012**, *6*, 11059–11065.

(8) Altantzis, T.; Goris, B.; Sánchez-Iglesias, A.; Grzelczak, M.; Liz-Marzán, L. M.; Bals, S. Quantitative Structure Determination of Large Three-Dimensional Nanoparticle Assemblies. *Part. Part. Syst. Charact.* **2013**, *30*, 84–88.

(9) Galván-Moya, J. E.; Altantzis, T.; Nelissen, K.; Peeters, F. M.; Grzelczak, M.; Liz-Marzán, L. M.; Bals, S.; van Tendeloo, G. Self-Organization of Highly Symmetric Nanoassemblies: A Matter of Competition. *ACS Nano* **2014**, *8*, 3869–3875.

(10) Zanaga, D.; Bleichrodt, F.; Altantzis, T.; Winckelmans, N.; Palenstijn, W. J.; Sijbers, J.; de Nijs, B.; van Huis, M. A.; Sánchez-Iglesias, A.; Liz-Marzán, L. M.; et al. Quantitative 3D Analysis of Huge Nanoparticle Assemblies. *Nanoscale* **2016**, *8*, 292–299.

(11) Wang, D.; van der Wee, E. B.; Zanaga, D.; Altantzis, T.; Wu, Y.; Dasgupta, T.; Dijkstra, M.; Murray, C. B.; Bals, S.; van Blaaderen, A. Quantitative 3D Real-Space Analysis of Laves Phase Supraparticles. *Nat. Commun.* **2021**, *12*, 3980.

(12) Altantzis, T.; Wang, D.; Kadu, A.; van Blaaderen, A.; Bals, S. Optimized 3D Reconstruction of Large, Compact Assemblies of Metallic Nanoparticles. *J. Phys. Chem. C* **2021**, *125*, 26240–26246.

(13) Wang, D.; Dasgupta, T.; van der Wee, E. B.; Zanaga, D.; Altantzis, T.; Wu, Y.; Coli, G. M.; Murray, C. B.; Bals, S.; Dijkstra, M.; et al. Binary Icosahedral Clusters of Hard Spheres in Spherical Confinement. *Nat. Phys.* **2021**, *17*, 128–134.

(14) Altantzis, T.; Zanaga, D.; Bals, S. Advanced Electron Tomography of Nanoparticle Assemblies. *Europhys. Lett.* **2017**, *119*, 38001.

(15) Udayabhaskararao, T.; Altantzis, T.; Houben, L.; Coronado-Puchau, M.; Langer, J.; Popovitz-Biro, R.; Liz-Marzán, L. M.; Vuković, L.; Král, P.; Bals, S.; et al. Tunable Porous Nanoallotropes Prepared by Post-Assembly Etching of Binary Nanoparticle Superlattices. *Science* **2017**, *358*, 514–518.

(16) Midgley, P. A.; Weyland, M. 3D Electron Microscopy in the Physical Sciences: The Development of Z-Contrast and EFTEM Tomography. *Ultramicroscopy* **2003**, *96*, 413–431.

(17) Batenburg, K. J.; Bals, S.; Sijbers, J.; Kübel, C.; Midgley, P. A.; Hernandez, J. C.; Kaiser, U.; Encina, E. R.; Coronado, E. A.; van Tendeloo, G. 3D Imaging of Nanomaterials by Discrete Tomography. *Ultramicroscopy* **2009**, *109*, 730–740.

(18) Batenburg, K. J.; Sijbers, J. DART: A Practical Reconstruction Algorithm for Discrete Tomography. *IEEE Trans. Image Process.* **2011**, *20*, 2542–2553.

(19) Chen, D.; Goris, B.; Bleichrodt, F.; Mezerji, H. H.; Bals, S.; Batenburg, K. J.; de With, G.; Friedrich, H. The Properties of SIRT, TVM, and DART for 3D Imaging of Tubular Domains in Nanocomposite Thin-Films and Sections. *Ultramicroscopy* **2014**, *147*, 137–148.

(20) Daniel, M.-C.; Astruc, D. Gold Nanoparticles: Assembly, Supramolecular Chemistry, Quantum-Size-Related Properties, and Applications toward Biology, Catalysis, and Nanotechnology. *Chem. Rev.* **2004**, *104*, 293–346.

(21) Kodaimati, M. S.; Lian, S.; Schatz, G. C.; Weiss, E. A. Energy Transfer-Enhanced Photocatalytic Reduction of Protons within Quantum Dot Light-Harvesting–Catalyst Assemblies. *Proc. Natl. Acad. Sci.* U. S. A. **2018**, *115*, 8290–8295.

(22) Hollingsworth, J. A.; Htoon, H.; Piryatinski, A.; Götzinger, S.; Sandoghdar, V. When Excitons and Plasmons Meet: Emerging Function through Synthesis and Assembly. *MRS Bull.* **2015**, *40*, 768–776.

(23) Jiang, R.; Li, B.; Fang, C.; Wang, J. Metal/Semiconductor Hybrid Nanostructures for Plasmon-Enhanced Applications. *Adv. Mater.* **2014**, *26*, 5274–5309.

(24) Fan, J. A.; Wu, C.; Bao, K.; Bao, J.; Bardhan, R.; Halas, N. J.; Manoharan, V. N.; Nordlander, P.; Shvets, G.; Capasso, F. Self-Assembled Plasmonic Nanoparticle Clusters. *Science* **2010**, *328*, 1135–1138.

(25) Klinkova, A.; Choueiri, R. M.; Kumacheva, E. Self-Assembled Plasmonic Nanostructures. *Chem. Soc. Rev.* **2014**, *43*, 3976–3991.

(26) Edel, J. B.; Kornyshev, A. A.; Urbakh, M. Self-Assembly of Nanoparticle Arrays for Use as Mirrors, Sensors, and Antennas. *ACS Nano* **2013**, *7*, 9526–9532.

(27) Li Volsi, A.; Fiorica, C.; D'Amico, M.; Scialabba, C.; Palumbo, F. S.; Giammona, G.; Licciardi, M. Hybrid Gold/Silica/Quantum-Dots Supramolecular-Nanostructures Encapsulated in Polymeric Micelles as Potential Theranostic Tool for Targeted Cancer Therapy. *Eur. Polym. J.* **2018**, *105*, 38–47.

(28) Roerdink, J. B. T. M.; Meijster, A. The Watershed Transform: Definitions, Algorithms and Parallelization Strategies. *Fundam. Inform.* **2000**, *41*, 187–228.

(29) Cao, M. Y.; Ye, C. H.; Doessel, O.; Liu, C. Spherical Parameter Detection Based on Hierarchical Hough Transform. *Pattern Recognit. Lett.* **2006**, *27*, 980–986.

(30) Paulano, F.; Jiménez, J. J.; Pulido, R. 3D Segmentation and Labeling of Fractured Bone from CT Images. *Vis. Comput.* **2014**, *30*, 939–948.

(31) Beucher, S.; Meyer, F. The Morphological Approach to Segmentation: The Watershed Transformation. In *Mathematical Morphology in Image Processing*; CRC Press, 1992; pp 433–481.

(32) Wang, Y.; Lu, T.; Li, X.; Ren, S.; Bi, S. Robust Nanobubble and Nanodroplet Segmentation in Atomic Force Microscope Images Using the Spherical Hough Transform. *Beilstein J. Nanotechnol.* **2017**, *8*, 2572–2582.

(33) Sato, Y.; Nakanishi, K.; Tanaka, H.; Sugano, N.; Nishii, T.; Nakamura, H.; Ochi, T.; Tamura, S. A Fully Automated Method for Segmentation and Thickness Determination of Hip Joint Cartilage from 3D MR Data. *Int. Congr. Ser.* **2001**, *1230*, 352–358.

(34) Glas, M. van der; Vos, F. M.; Botha, C. P.; Vossepoel, A. M. Determination of Position and Radius of Ball Joints. *Proc. SPIE*; **2002**, *4684*, 1571–1577.

(35) Ye, X.; Zheng, C.; Chen, J.; Gao, Y.; Murray, C. B. Using Binary Surfactant Mixtures to Simultaneously Improve the Dimensional Tunability and Monodispersity in the Seeded Growth of Gold Nanorods. *Nano Lett.* **2013**, *13*, 765–771.

(36) Grzelczak, M.; Sánchez-Iglesias, A.; Liz-Marzán, L. M. A General Approach toward Polymer-Coated Plasmonic Nanostructures. *CrystEngComm* **2014**, *16*, 9425–9429.

(37) Gorelikov, I.; Matsuura, N. Single-Step Coating of Mesoporous Silica on Cetyltrimethyl Ammonium Bromide-Capped Nanoparticles. *Nano Lett.* **2008**, *8*, 369–373.

(38) Moon, T. K. The Expectation-Maximization Algorithm. *IEEE Signal Process. Mag.* **1996**, *13*, 47–60.

(39) Dempster, A. P.; Laird, N. M.; Rubin, D. B. Maximum Likelihood from Incomplete Data via the EM Algorithm. *J. R. Stat. Soc. Series B* **1977**, *39*, 1–22.

(40) Levitan, E.; Herman, G. T. A Maximum a Posteriori Probability Expectation Maximization Algorithm for Image Reconstruction in Emission Tomography. *IEEE Trans. Med. Imaging* **1987**, *6*, 185–192.

(41) Hough, P. V. C. Method and Means for Recognizing Complex Patterns. 3,069,654, 1962.

(42) De, S.; Biswas, N.; Sanyal, A.; Ray, P.; Datta, A. Detecting Subsurface Circular Objects from Low Contrast Noisy Images: Applications in Microscope Image Enhancement. *World Acad. Sci. Eng. Technol.* **2012**, *67*, 1317.

(43) Töpperwien, M.; van der Meer, F.; Stadelmann, C.; Salditt, T. Three-Dimensional Virtual Histology of Human Cerebellum by X-Ray Phase-Contrast Tomography. *Proc. Natl. Acad. Sci.* U. S. A. **2018**, *115*, 6940–6945.

(44) Balzan, R.; Sellerio, A. L.; Mari, D.; Comment, A. High-Precision MRI Reconstruction Algorithm for 3D Sphere Packings. *Appl. Magn. Reson.* **2015**, *46*, 633–642.

(45) Memiş, A.; Varlı, S.; Bilgili, F. Computerized 2D Detection of the Multiform Femoral Heads in Magnetic Resonance Imaging (MRI) Sections with the Integro-Differential Operator. *Biomed. Signal Process. Control* **2019**, *54*, 101578.

TOC Graphic